Role of limestone micro-porosity on dissolution patterns during reactive transport with carbonated water

Matthieu Mascle[1*], *Hervé Deschamps*[1], *Souhail Youssef*[1], *Fadi Nader*[1]

[1]IFP Energies Nouvelles, 1 et 4 avenue de Bois-Préau, 92852 Rueil-Malmaison, France

Abstract. In this work, we have investigated the effect of two different limestone textures (namely Lavoux and Euville limestone) on the reactive transport. These two rock-types have a similar chemical composition (pure calcite) but differ by their macro- and micro-structures. An extensive workflow of experiments has been carried out to characterize the macro- and micro-porous systems of the cores, and to understand the interaction between the different properties that are relevant for the reactive transport. It includes 5 µm pixel resolution 3D scans of the cores and miscible tracer injections conducted before and after the alteration. Core alteration has been conducted using carbonated water to be more representative of CO_2 storage conditions. Experiments have been conducted at ambient temperature (25°C) and at 10 bar of pore pressure. Results have shown that Lavoux limestone has higher micro-porosity and better-connected grains than Euville limestone. Mass transfer of the reactive fluid in the micro-porosity, where most of the reactive surfaces are, is limited for Euville. Consequently, Lavoux limestone showed a more homogeneous and sustained dissolution front, while Euville developed early breakthrough and localized. The two cores initial flow properties have been altered to a completely different extent. The absolute permeability has been multiplied by more than 100 for Euville core, while it has been increased by less than 2 for Lavoux core.

1 Introduction

According to a recent report from the Intergovernmental Panel on Climate Change (IPCC), the objective of limiting the global warming to +1.5°C can only be reached by removing tens of giga-tons of CO_2 per year ($GtCO_2$/yr) from the atmosphere [1]. Many publications [2–4] have reviewed the different technologies that need to be used to address this objective. Among them, sequestration of CO_2 into subsurface geological formations is the most mature technique, accounting today for roughly 4 mega-tons of CO_2 per year ($MtCO_2$/yr) [2].

When injected into underground geological formations, the primary trapping mechanism for CO_2 is the geology structure and stratigraphy. The CO_2 migration to the surface is prevented by a reservoir seal: a geological formation characterized by a high capillary pressure and a low permeability. The secondary trapping mechanisms involve the capillary trapping of CO_2 in the porous reservoir and its solubilization in the brine [5]. The later (CO_2 solubilization in brine) has two consequences: (1) the acidification of the brine in contact with the CO_2 and (2) an increase in the brine density because of the CO_2 solubilization. At the reservoir scale, this acidification and the brine density increase mainly occur at the interface between the stratigraphically trapped CO_2 plume and the brine aquifer above which it accumulates. This results in the destabilization of the upper layers of the aquifer by gravity, with heavier and acidified brine being carried downward and 'fresh' water rising towards the caprock [6]. This density-driven flow is an important mechanism in CO_2 storage as it promotes the distribution of dissolved CO_2 in the deeper reservoir layers, but it also impacts the geological formations it flows through. In the case of carbonate rocks, the circulation of acidified brine leads to their gradual dissolution [7] with complex dissolution patterns specific to the flow conditions, to the rock properties and to the fluids. In return, the dissolution alters the initial properties of the geological formation, such as its flow properties, its storage properties or its geo mechanical properties.

Reactive transport in porous medium is a multi-physics problem, that requires understanding (1) the transport of the reactive fluid in the core, (2) the chemical reactions involved, and (3) the core properties relevant for the chemical reactivity. The dissolution pattern developing in a core is a balance between how far the reactive fluid is transported through the core (by convection or diffusion mechanism), versus how fast it reacts with the rock before being equilibrated. The Péclet and Damköhler classification has been widely used to predict and classify the dissolution regimes for given

* Corresponding author: matthieu.mascle@ifpen.fr

experimental conditions of injection, fluids and rocks [8, 9]. The different dissolution patterns (compact, wormhole or uniform) have been initially explained by convection-limited, mass transport-limited or reactive surface-limited regimes. Many modifications of this classification have been suggested in the literature, to account for more pattern types [10, 11] or to modify the expression of the dimensionless numbers [12]. The Péclet and Damköhler classification is a useful tool to understand the effect of the different conditions and parameters on the reactive transport outcome. Its main flaws are that (1) the two dimensionless numbers used are not temporally and spatially constant or homogeneous throughout the experiment; and (2) some of their parameters involved need an extensive understanding of the fluid transport in the porous media to be correctly defined. This is especially the case of the characteristic length. As argued by [10], it should be representative of the fluid transport at the pore scale. However, carbonate rocks typically exhibit complex macro- and micro-porous architectures with differing scales and properties, leading to a non-trivial interplay that challenges predictive modeling.

In this work we have applied an extensive workflow of experiments to understand this interplay for two rocks: Lavoux and Euville limestone. These two rock-types have a similar chemical composition but differ by their macro and micro-structures. The latter have been characterised using 3D tomographies, miscible tracer displacements and numerical simulations. The reactive transport has been performed using carbonated water to be more representative of CO_2 storage conditions. The main objectives here are to compare the effect of the porous structures alone on the reactive transport and to understand what the driving features.

2 Materials and methods

2.1 Limestone Characterization

Two French quarry limestones have been used in this study, namely Lavoux and Euville limestone. Lavoux limestone is from Oxfordian age and the Eastern Paris Basin, Euville limestone is from Bathonian age and the Poitou-Charentes. These two have been chosen because they have a comparable chemical composition: almost pure calcite (>98mol% $CaCO_3$) [12], enabling the same chemical reactions to occur during the reactive transport. 2 mini plugs have been used in this study, suitable for the coreflood platform CAL-X™ [13]. Approximate plug length (L) and diameter (D) are respectively 20 mm and 10 mm. The main cores characteristics are given in Table 1. The core's porosities (ϕ_{tot}) have been measured using the weighting method (dry and saturated with brine) and the core's absolute permeabilities (K_w) have been measured with brine. All experiments have been conducted on these two plugs.

Table 1: Cores main characteristics before alteration.

Sample	Lavoux	Euville
L, D (mm, mm)	20.3, 9.6	20.5, 9.7
K_w (md)	130	33
ϕ_{tot}	25%	20.4%
Pore volume (cc)	0.367	0.309

The two limestone fabrics can be observed in Fig. 1. They are defined as grainstones, composed of cemented elements, varying by their size and nature. For Euville sample, these elements are mostly crinoid's fragments (crowns and stalks), while the Lavoux is composed of ooids. The space between these elements (crinoids or ooids) is the inter-granular porosity, also referred in this work as the macro-porosity. Inside those grains, an intra-granular porosity can be guessed, referred here as the micro-porosity. In Fig. 1, this micro-porosity is largely under the 5 µm pixel resolution and therefore cannot be directly observed, but it translates on these images as gray levels variations. Euville limestone has overall larger grains than the Lavoux, leading to less but wider macro-pores. Yet, the core's absolute permeabilities have been measured to 33 mD and 130 mD respectively, suggesting a key role of the micro-porosity system in the fluid transport. Additional observations and characterization of these microstructures using NMR and MICP can be found on colleagues' paper [12].

From these first observations, it shall be retained that despite having the same chemical composition, the two samples came from different depositional environments leading to different porous medium construction. One of the main objectives of this study is to characterize both the macro- and micro-porosity systems in detail, using tomographic and radiographic data, and to understand their respective roles in the reactive transport process.

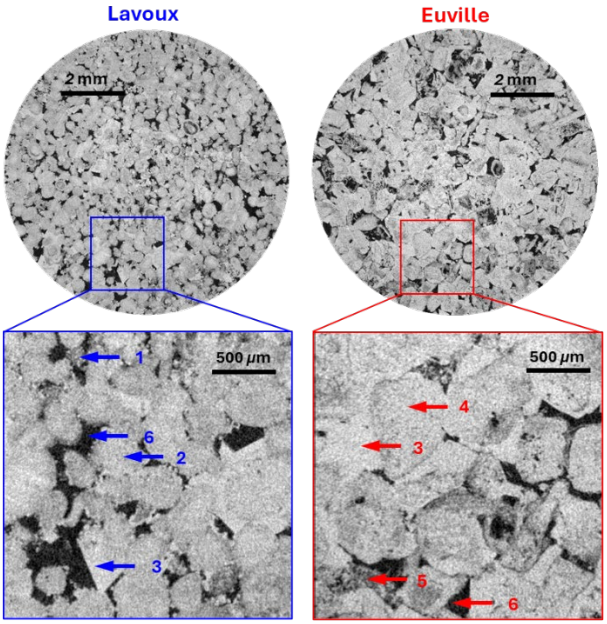

Fig. 1: 3D tomographies (5 µm resolution) of the two Lavoux and Euville limestones (left and right respectively). Arrows indicate equant cement (1), porous ooid (2), syntaxial cement

(3), porous crinoid's stalk (4), porous crinoid's crown (5) and voids (or macro-pores) (6).

2.2 3D Tomography

The two mini plugs have been scanned in dried state at 5 µm pixel resolution before and after alteration. Final reconstructed volumes have 1950*1950*4200 pixels dimensions, and they are written in 16 bits (grey values range from 0 to 65535). Acquisitions were made at 100 KeV and 50 mA, using a 100 µm tin filter to mitigate beam hardening. These 3D scans have been used to characterize the cores micro- and macro-porosity systems, and to observe evidence of the dissolution at local and core scale.

The scans have been post-treated to reduce noise, using a block-matching and 3D-filtering filter (BM3D) [14]. Grey values of the four scans (Euville and Lavoux before and after alteration) have been corrected and normalized so they can be quantitatively compared with each other. The main difficulty here is to identify two reference values for the normalization. The grey values in the macro-porosity and in the syntaxial cement (see arrow 3 in Fig. 1) have been used as references for normalization. Syntaxial cement has the advantage of being compact calcite (almost no micro-porosity), allowing to be compared from one scan to another. All other solid materials are micro-porous and therefore cannot be used for the normalization as their micro-porosity is not known a priori. The first reference (macro-pores) is easily measured for the four scans (NG_1), as its grey pic value stands out in all the grey values distributions (Fig. 2). The second one (syntaxial cement) is more difficult to measure due to its limited occurrence in the cores, and its proximity (in grey value) with all other micro-porous materials. Its grey value pic (NG_2) can be isolated when choosing a sub-volume containing a large calcite crystal (Fig. 2). Technically, this normalization using the NG_1 and NG_2 values converts a grey value into a porosity value computed at the pixel resolution, but the conversion is too noisy to compute a pixel porosity value. As we are working on 16 bits images, these NG_1 and NG_2 are set to 0 and 1 but to 15000 and 40000.

The last step of the post-processing is the spatial alignment of the scans before and after alteration. This step is performed using AVIZO software.

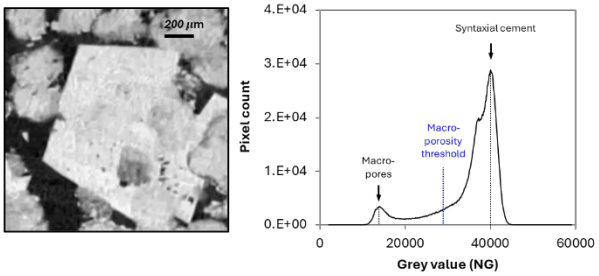

Fig. 2 : Sub-volume of the Lavoux 3D tomography centered on a large calcite crystal (left), with its grey value distribution (right). The two black lines indicate the macro-pores and syntaxial cement pics used for the normalization (NG_1 and NG_2 respectively, set to 15000 and 40000). The blue line indicates the threshold used when segmenting the macro-porosity from the matrix.

In addition to a general description of the core's micro-structures, the 3D data sets have been used to quantify the different pore systems of the cores. The macro-porosity value is easily computed by applying a threshold value between the macro-pores and the solid materials (micro-porous grains and cement) (see blue arrow in Fig. 2). The micro-porosity cannot be directly computed here due to the limited grey contrast between the syntaxial cement and the porous grains. But the total porosity (ϕ_{tot}) is given when normalizing the grey value (NG) between the two reference values mentioned below (NG_1 and NG_2 for the macro-pores and the syntaxial cement) (see Eq. 1). This computation can be performed for each slice, enabling the measurement a vertical porosity profile all along the core. The micro-porosity profile is then deduced using the total and macro-porosity profile.

$$\phi_{tot} = \frac{NG - NG_1}{NG_2 - NG_1} \qquad \textbf{Eq. 1}$$

The computations described here only are only valid because the samples are almost pure calcite. The grey values are only a function of the porosity and not of the mineralogy. It should also be kept in mind that no concern of the porosity systems connectivity is considered when interpreting the tomography data. This aspect is addressed during the tracer experiments, with the interpretation of the 2D radiographies.

2.3 Coreflood experiments

2.3.1 Coreflood setup

Two types of coreflood experiments have been conducted on these cores: the reactive injection itself to alter the core, and monophasic tracer injections run before and after the alteration. The experimental setup CAL-X™ has been used to run these experiments. Technical information regarding the setup can be found on previous published works [13, 15]. A mentioned above it uses 2 cm long cores, and the fluid saturation is computed through the interpretation of 2D radiographies taken every 10 seconds, at 60 KeV, 500 mA and 30 µm pixel resolution (see Fig. 3 and Fig. 4). The radio monitoring is different from the tomography as all radiographies are taken from the same angle and perspective. Each pixel sums the attenuation of all material crossed by the X-Ray, from the emitting point to the detector. The Beer-Lamber X-Ray attenuation law (I) for multi-materials system is used here to relate the measured X-Ray intensity (I) with the columns x_i of phases crossed and their respective attenuation coefficient μ_i (Eq. 2).

$$\log(I) = -\sum_i x_i * \mu_i, \qquad \textbf{Eq. 2}$$

Their interpretation is made by subtracting one radiography (used as reference) to all other radiographies.

The result shows the differences of X-Ray attenuation in the core, compared to this reference radiography. Those differences occur when one fluid is replaced by another (tracer test for example), or when the solid phase is replaced by a fluid (dissolution experiment for example). It is expressed as a grey value variation, and it is function of the attenuation contrast between the two fluids (or one fluid and the solid phase), and the quantity of fluid (or solid) replaced. When working with a two phases system (two phases changing), these grey value variations can be translated into a fluid saturation, a tracer quantity or a porosity creation. Additional explanations regarding the interpretation of the X-Ray 2D radiographies can be found amongst others in previous work [16].

When mounted the core in the Hassler cell, aluminum foil is used to prevent dissolved CO_2 to diffuse in the sleeve. A 2 mm thick inlet piece (diffuser) is also used at the core entry to mitigate injection artefact and to favor homogeneous injection boundary conditions. The core is set in vertical position (z axis), and fluids are injected from bottom to top. Experiments are conducted at ambient temperature (25°C), with 30 bar of confining pressure (P_{conf}) and 10 bar of pore pressure (P_{pore}). To avoid undesired rock alteration during the non-reactive experiments, all injected fluids (except for the carbonated water) were degassed under vacuum and equilibrated with finely crushed Lavoux or Euville limestone powder. This pre-equilibration ensures that the injected fluids are near chemical equilibrium with the host rock, thus minimizing any dissolution during characterization.

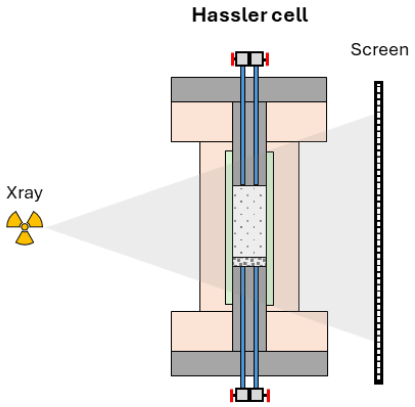

Fig. 3: Schematic view of CAL-X™ Hassler cell.

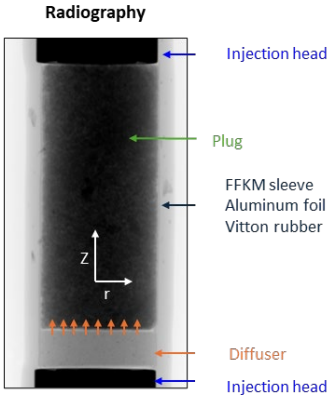

Fig. 4: 2D radiography of the core mounted in the Hassler cell.

2.3.2 Passive tracer test

The passive tracer experiments are performed by injecting a 150 g/L KBr solution at 0.1 cc/min in the core previously saturated with deionized water. A total of 12 PV and 21 PV have been injected during the Lavoux and Euville tracers, respectively. The density contrast of the fluids is captured by the X-Ray monitoring, as the KBr solution attenuates more the X-Ray than the deionized water. It allows to qualitatively assess the displacement homogeneity and to quantitatively measure the volume of porous medium invaded during the tracer test. By comparison to the 3D tomography, the tracer test monitoring provides information regarding the connected total porosity. These radiographies are used here to compute the KBr tracer curves $S_{KBr}(t)$ using Eq. 3, and the total porosity profile $\phi_{tot}(z)$ using Eq. 4. In Eq. 3, I_t, I_{water} and I_{KBr} are respectively the average core X-Ray intensity measured at time t, and when the core is saturated with deionized water with the KBr solution. In Eq. 4, $I_{water}(z)$ and $I_{KBr}(z)$ are respectively the X-Ray intensity (at the z position) when the core is saturated with deionized water or with the KBr solution.

$$S_{KBR}(t) = \frac{\log(I_t) - \log(I_w)}{\log(I_{KBr}) - \log(I_w)} \qquad \textbf{Eq. 3}$$

$$\phi_{tot}(z) = \frac{\log(I_{KBr}(z)) - \log(I_w(z))}{\log(I_{KBr}) - \log(I_w)} * \phi_{tot} \qquad \textbf{Eq. 4}$$

The tracer data are also used is to assess the contribution of the micro-porosity to the flow. A lower contribution to the flow would translate in these tracer curves as a longer end-tail production. This is performed by history-matching the measured average core saturation. The commercial solution CYDAR® (http://cydarex.fr/) has been used to run the simulations, with Coats and Smith's dead-end and pore-volume dispersion model [17]. This model accounts for a main well-connected porous system where dispersion occurs in the flowing direction (D_z); and for dead-ends volumes. A simple mass transfer equation allows these stagnant zones to be filled by the tracer. It is function of the tracer concentration gradient between the stagnant and the non-stagnant zones and a transfer coefficient K_s in s^{-1}. For our samples, the stagnant and non-stagnant zones can be used to respectively describe the micro- and macro-porosity systems. The major assumption made here is to describe the micro-porous grains as dead-ends. This assumption is believed to be not valid, but it is also reasonable to assume that the grains permeability is orders of magnitude lower than the core permeability. Therefore, the transport in those grains is not mainly dispersive as it is in the macro-pores, but a combination of dispersion and diffusion. The history match performed here only aims at comparing the micro- and macro porosity systems connectivity, using a simple coefficient, namely the K_s transfer coefficient in this model.

2.3.3 Core alteration with carbonated water

Carbonated water has been injected to alter the core by dissolution. Injection is performed at 0.1 cc/min. It is prepared by equilibrating gaseous CO_2 (gas) with deionized water at P_{pore} (10 bar) and ambient temperature. In these conditions, the brine is at pH = 3.4, and the carbonic acid equilibrium is given in Table 2.

Calcite dissolution in carbonated water is a first order reaction, whose rate R_{diss} and kinetic v_{diss} (in mol/m²/s and mol/s respectively) is given by Eq. 5 [7]. The dissolution is driven by 3 distinct contributions, described in Eq. 6. In Eq. 5, k_j and a_i are respectively the reaction constant and the activity coefficient; and S_{react} is the surface of calcite available (and accessible) for the reaction.

Table 2: Carbonic acid equilibrium in deionized water, at 25°C and P_{CO2} = 10 bars.

	$[CO_3^{2-}]$	$[HCO_3^-]$	$[CO_{2(aq)}]$
[mmol/L]	0	0.4	340

$$R_{diss} = k_1 + k_2 * a_{H^+} + k_3 * a_{CO_{2,aq}} \qquad \textbf{Eq. 5}$$
$$v_{diss} = R_{diss} * S_{reac}$$

$$\begin{cases} CaCO_3 \overset{k_1}{\leftrightarrow} Ca^{2+} + CO_3^{2-} \\ CaCO_3 + H^+ \overset{k_2}{\leftrightarrow} Ca^{2+} + HCO_3^- \\ CaCO_3 + CO_{2,aq} + H_2O \overset{k_3}{\leftrightarrow} Ca^{2+} + 2HCO_3^- \end{cases} \qquad \textbf{Eq. 6}$$

3 Results

3.1 Petrophysical characterisation before alteration

3.1.1 Static characterisation

Grey levels distributions of the Lavoux and the Euville samples are compared in Fig. 5. These two distributions have been corrected considering the peak values for macro-pores and cement (Fig. 2). Therefore, differences in these two distributions reveal differences in the two samples micro- and macro-structures. Euville's macro-pore peak is more pronounced than the Lavoux's one (and comparably spread), suggesting a higher macro-porosity (ϕ_{macro}) for the Euville, while having a lower total porosity (see ϕ_{tot} in **Table 1**). Its matrix grey levels distribution (porous grains and cement) is overall shifted toward higher grey values compared to the Lavoux, suggesting overall less micro-porous grains (ϕ_{micro}).

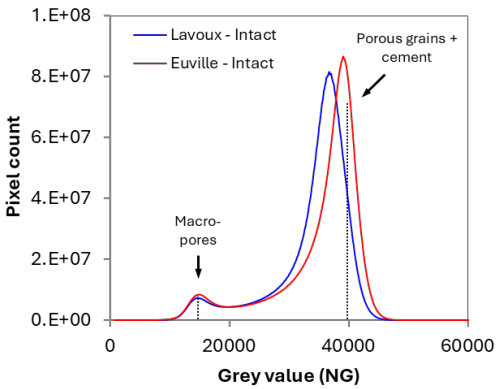

Fig. 5: Grey values distribution of the Lavoux (blue) and Euville (red) samples. Macro-pores and calcite cement (NG_1 and NG_2) are respectively set to 15000 and 40000.

The three porosities (ϕ_{tot}, ϕ_{macro}, and ϕ_{micro}) are quantified using the 3D scans at the core and slice scales (Table 3 and Fig. 6). The average total porosity ϕ_{tot} is measured to 23.7% and 19.3% for the Lavoux and the Euville respectively, which is consistent with the values obtained using the weighting method (see Table 1). Euville has a slightly higher average macro-porosity ϕ_{macro} than the Lavoux (16.2% for the Euville, 14.9% for the Lavoux), and a substantially lower average micro-porosity ϕ_{micro} (3.1% for the Euville and 8.2% for the Lavoux). Overall, the two samples have a comparable macro-porosity, but the Lavoux has almost 3 times more micro-porosity. This observation suggests that, despite the lower macro-porosity, the better-connected or more accessible microporous system in the Lavoux might significantly contribute to fluid transport (see Fig. 1). These results obtained through images interpretation are overall comparable to measurements performed using other techniques [12]. Yet, differences exist as carbonate rocks can exhibit high degree of heterogeneities and even sister plugs can show substantial differences in porosity distributions.

The vertical ϕ_{tot} and ϕ_{macro} profiles are shown in Fig. 6 (blue/red and grey curves respectively). They show moderate heterogeneities all along the cores, that are mostly explained by the macro-porosity. The micro-porosity ($\phi_{tot} - \phi_{macro}$) appears more homogeneously distributed all along the cores. These profiles, computed using 3D images segmentations, do not account for connectivity (or percolation) among these porosity systems. Some of the porosity contained in the micro-porous grains might not be connected to the main porosity system. This aspect is addressed using the miscible tracer experiment monitored using the radiographies. The vertical porosity ϕ^z_{tot} profile is derived from it (see Eq. 4) accounting for all the pore space invaded during the displacement (i.e. connected). This profile is plotted in Fig. 6 (black dashed curve) and shows a good match for both the Euville and the Lavoux with the total porosity profile computed from the 3D tomography. Minor differences between the two total porosity profiles can be observed, but they can be explained by (1) the difference of spatial resolution acquisitions, and (2) a perspective effect for the radiography, especially near the core's top

and bottom. Overall, this comparison suggests that the entire micro-porosity system is connected to the macro-porosity system, as it is flooded during the tracer experiment.

Table 3 : Average ϕ_{tot}, ϕ_{macro}, and ϕ_{micro} values computed on the Lavoux and Euville limestones from the 3D scans.

	Lavoux	Euville
ϕ_{tot}	23.7%	19.3%
ϕ_{macro}	14.9%	16.2%
ϕ_{micro}	8.8%	3.1%

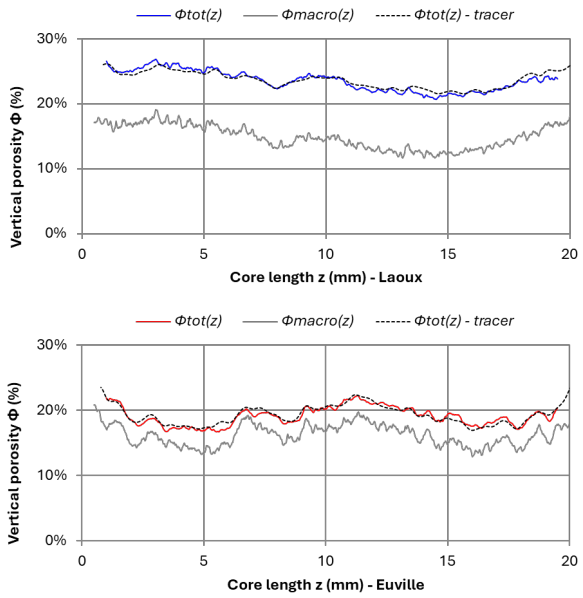

Fig. 6: Lavoux (top) and Euville (bottom) ϕ_{tot} and ϕ_{macro} vertical profiles, computed from the 3D scans. The dashed line ϕ_{tot} (tracer) is computed from the tracer experiment (Eq. 3).

3.1.2 Dynamic characterisation

The tracer experiments have been performed by injecting a 150 g/L KRr solution in the samples, at 0.1 cc/min. Results of the displacement are shown in Fig. 8 with 2D saturations maps taken during the early steps of the KBr invasion. The tracer curves are also compared for the two samples in Fig. 7.

Characterizing the displacement homogeneity using these data is difficult without numerical tools. Fig. 8 shows saturation maps taken during the first steps of the tracer invasion. For the two cores, the tracer breakthrough (BT) can be observed before 2 min of injection. The tracer saturation profiles taken every 10 seconds (not shown here) reveal it occurs when the Lavoux and the Euville are saturated with the KBr solution at S_{KBr}(BT) = 19% and S_{KBr}(BT) = 23%, respectively. This early BT is explained by the dual porosity system, leading to a preferential invasion of the macro-porous system and a delayed invasion of the micro-porous system. The saturation maps also suggest a more homogeneous displacement for the Euville, with less saturation contrast in the radial direction. For the Lavoux sample, the saturation maps show higher tracer concentrations at the center the core. This might result from local permeability variations (with statistically higher permeabilities at the core center), or by a laboratory artefact leading to a preferential entry point (despite actions taken to avoid that). After BT, the tracer curves (Fig. 7) slowly reach a stable value, equal here to the core's PV. Lavoux's core is saturated quicker than Euville's one, while having a bigger PV. While the saturation measured at BT provides information regarding dispersion in the macro-porosity, the tracer's tail shows how the mass transfer occurs between the micro- and the macro-pores. These first observations suggest a lower connectivity for the Euville, as it takes more time to fully saturate the core.

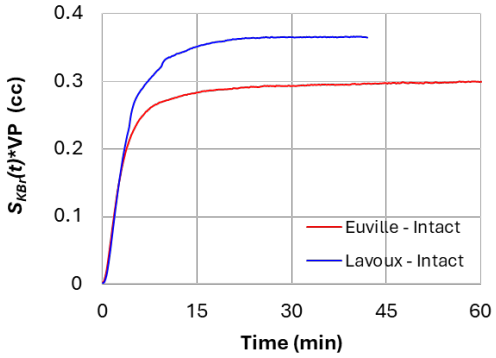

Fig. 7: Tracer curves $S_{KBr}(t)$*VP during the miscible injection of the 150 g/L KBr solution, for the Lavoux (blue) and Euville (red) samples.

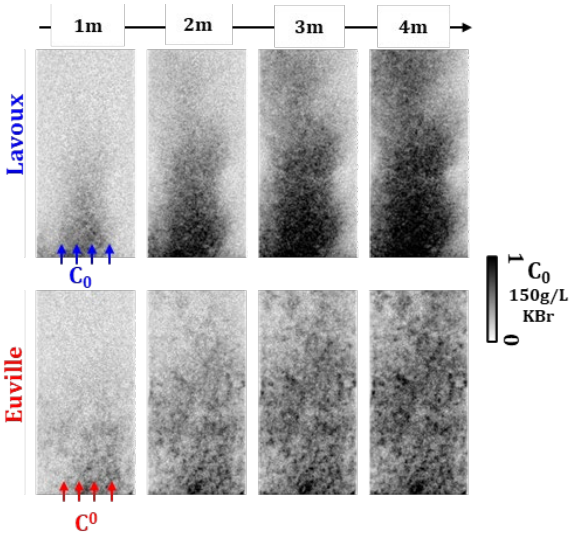

Fig. 8 : 2D saturation maps (radiography monitoring) during the first steps of the tracer injections for the Lavoux (top) and the Euville (bottom) samples. Injection is performed vertically from bottom to top. Darker shades indicate higher tracer concentrations.

The tracer experiments have been history matched using Coats and Smith's dead-end and pore-volume dispersion model [17]. Two parameters are fitted here: the tracer dispersion (D_z) in the macro-porosity system and the mass transfer coefficient K_s between the micro- and the macro-porosity systems. Results of the history match are shown in Fig. 9, with the two fitted parameters given

in Table 4. The two samples dispersity (characterizing the macro-porosity-system) are rather high but comparable (0.32 cm and 0.25 cm for the Lavoux and the Euville respectively). The K_s coefficient, quantifying the mass transfer between the micro-pores (described as dead-ends in this model) and the macro-porosity systems, shows a strong contrast between the two samples. It is order of magnitude higher for the Lavoux than for the Euville (1.77 min^{-1} for the Lavoux compared to 0.076 min^{-1} for the Euville). This suggests that the microporous grains in Lavoux are more accessible and contribute more significantly to flow, resulting in a higher apparent mass transfer coefficient. It should be noted that the numerical model used here for the fitting process assumes a dead-end micro-porous system, which is not a valid assumption for these two limestones. It has already been mentioned above that the micro-porous grains were probably contributing substantially to the flow for the Lavoux limestone. Therefore, the D_z and K_s values obtained here cannot be compared with other published work.

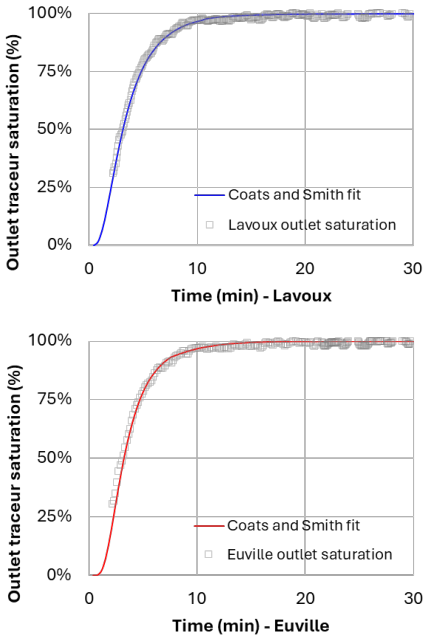

Fig. 9: Outlet tracer concentration fitted using Coats and Smith dead-ends and pore-volume dispersion model. The fitted parameters are the macro-porosity dispersion D_z and the transfer coefficient K_s between the macro- and the micro-porosity (Table 4). The fit mean squared error (MSE) is below $3*10^{-2}$ for the two simulations.

Table 4 : Coats and Smith fitted parameters for the tracer experiments.

	Lavoux	Euville
D_z (cm)	0.32	0.25
K_s (min^{-1})	1.77	0.076

3.2 Dissolution reaction kinetic

The equilibration of the injected carbonated water with calcite has been estimated using the free version of aqion simulator (see Table 5). When equilibrated with calcite, the reactive brine pH is increased of 2 units from pH = 3.4 to pH = 5.4, and the quantity of dissolved Ca^{2+} is calculated to 18.8 mmol/L (or ~750 mg/L of Ca^{2+}). As the equilibrated brine pH stays lower than 6.4 (first carbonic acid's pK_a), most of the carbonic acid is in $CO_{2(aq)}$ form. If the reaction occurs faster than the transport of the reactive fluid in the core (i.e. if the fluid is equilibrated before BT), then a dissolution rate at equilibrium v_{diss}^{eq} can be estimated using a direct volume balance. When considering the carbonated water injection flow rate of 0.1 cc/min, v_{diss}^{eq} is estimated to $3.1*10^{-8}$ mol/s. v_{diss}^{eq} can be interpreted as a transport-limited dissolution rate. It is therefore identical for Lavoux and Euville, as the reactive fluid is injected in the same conditions for the two cores.

Table 5: Simulated equilibrated brine composition in contact with calcite, using aqion simulator. Initial brine is prepared with 10 bars of CO_2 at 25°C.

	$[Ca^{2+}]$	$[CO_3^{2-}]$	$[HCO_3^-]$	$[CO_{2(aq)}]$
[mmol/L]	18.8	0	0.42	317

The calcite dissolution kinetic for our system is given by Eq. 5. It only applies at t = 0 as this formulation doesn't account for the accumulation of the reactions' products (Ca^{2+}, HCO_3^- and CO_3^{2-}). The previous equilibrium analysis has shown that only Ca^{+2} accumulates in the reactive fluid, as HCO_3^- and CO_3^2 are converted into $CO_{2(aq)}$. The three reaction constants k_1, k_2 and k_3 are given to $1.2*10^{-7}$, $5.1*10^{-2}$ and $3.5*10^{-5}$ respectively, at 25°C using equations 5, 7 et 8 from [7].These values tell us which of the three reactions drives the calcite dissolution depending on the solution pH. The first reaction (k_1) is constant and is neglectable due to its extremely low k_1 value. The second reaction (k_2) has a very high reaction constant (compared to k_1 and k_3) and is function of the solution pH. The reaction kinetic is divided by 100 when the pH is increased from its initial value (pH = 3.4) to its equilibrated value (pH = 6.4). The third reaction (k_3) is overall constant for our system as the solution pH stays below pH = 6.4: the $CO_{2(aq)}$ concentration is only reduced by 8% during the reaction of equilibration with calcite. Its reaction constant k_3 is substantially lower than k_2 but the reaction is promoted by the high $CO_{2(aq)}$ concentration (see Table 2). At t = 0 (pH = 3.4), the calcite dissolution rate is computed to $R_{diss} = 3.2*10^{-4}$ mol/m²/s, with 65% of the dissolution being driven by the second reaction (k_2). When the pH is increased to pH = 6.4, the third reaction (k_3) quickly become dominant.

Lavoux and Euville specific surfaces S_{spec} have been measured on small 4 mm diameter and 6 mm long sister plugs. Measurement have been performed using krypton adsorption and BET modelling [18]. S_{spec} has been measured to 0.539 m^2/g and 0.238 m^2/g for Lavoux and Euville respectively. Lavoux's specific surface is almost two times Euville's one, which agrees with its higher micro-porosity value (Table 3). When taking S_{reac} as the total core surface ($S_{reac} = S_{spec} * m_{plug}$) as a first assumption (with m_{plug} the core dry mass), v_{diss}^{spec} is computed to $5.0*10^{-5}$ mol/s and $2.4*10^{-5}$ mol/s for Lavoux and Euville

respectively (Table 6). Unlike v_{diss}^{eq}, v_{diss}^{spec} can be interpreted as surface-limited dissolution rate, accounting the cores' micro-structures. Its computation assumes that all the core surface is available for the reactions (and constant) and in contact with fresh reactive fluid ($[Ca^{2+}] = 0$). It is safe to say that this dissolution rate has no reality for our experiments, otherwise the cores would be entirely dissolved within 2 minutes of injection. Yet, this result tells us one important aspect of the reactive transport for our system. The core scale dissolution rate will be limited by the injection of reactive fluid in the core at least during the early steps of the injection (before BT). But locally, the dissolution rate will be driven by the accessible reactive surface, potentially twice faster for Lavoux than for Euville due to its higher specific surface.

Table 6 : Dissolution kinetics computed using Eq. 5.

	Lavoux	**Euville**
S_{spec} **(m²/g)**	$5.39*10^{-1}$	$2.38*10^{-1}$
m_{plug} **(g)**	2.86	3.09
S_{reac} **(m²)**	1.54	0.74
R_{diss} **(mol/m²/s)**	$3.2*10^{-5}$	
v_{diss}^{spec} **(mol/s)**	$5.0*10^{-5}$	$2.4*10^{-5}$

3.3 Reactive transport characterisation

The reactive transport has been performed by injecting the carbonated water (see Table 2) during 16h for the Lavoux and 20h for the Euville, at 0.1 cc/min. Injection has been stopped earlier for the Lavoux due to the sample failure near the entry. The core's alteration has been monitored with the radiography monitoring during the injection and the samples have been scanned at 5 µm pixel resolution at the end of the experiment.

Fig. 10 shows the cumulative and derivative mass of calcite dissolved during the alteration experiment. These values are derived from the interpretation of the X-Ray radiographies and the final core's porosity estimated with the 3D tomography. After 16h of injection, the total quantity of calcite dissolved is higher for the Lavoux than for the Euville. It is calculated to 86 µg for the Lavoux (around 3% of its initial mass) and to 64 µg for the Euville (around 2.1% of its initial mass) in Fig. 10. Yet, during the early steps of the alteration (< 4h), the dissolution rate (in mg of $CaCO_3$ per liter of carbonated water injected) is comparable for the two samples (~ 700 mg/L, or 17.5 mmol/L). After 4h of injection, it decreases for the Euville while it is maintained overall constant for the Lavoux. The higher values observed for the Lavoux (> 750 mg/L) are explained by an underestimation of the volume of fluid injected in the core, due to a small exsolution of gaseous CO_2 in the injection line. After 16h of injection, the dissolution rate for the Euville has been reduced by more than 2.

The dissolution patterns shown in Fig. 11 explain the lower dissolution rates observed for the Euville after 4h of injection. As the carbonated water is injected, the dissolution slowly rises in the cores, moving toward the core's outlet. The latter is reached after 4h of injection for the Euville, while it hasn't within the 16h of injection for the Lavoux. Before the breakthrough, the dissolution rate is therefore the same for the two cores when computed at the core scale. But it is locally higher for the Lavoux, reducing the dissolution front migration. Once the dissolution pattern breaks through for the Euville, a fraction of the reactive fluids is transported through the core without enough time to equilibrate with the calcite, lowering the dissolution rate at the core scale.

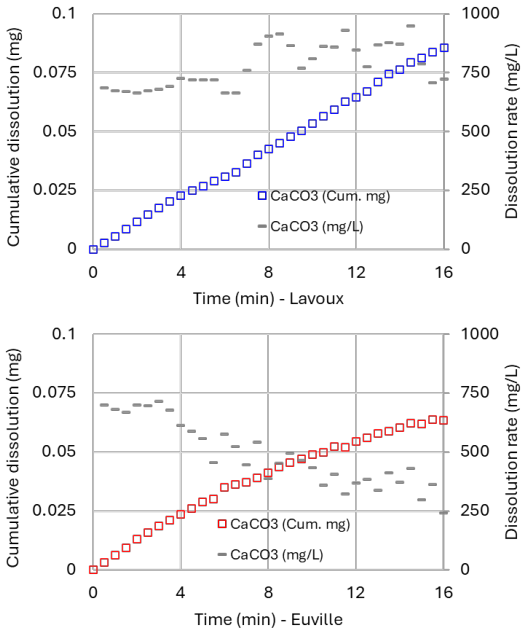

Fig. 10: Cumulative (mg) and derivative mass (mg/L) of dissolved $CaCO_3$ computed for the Lavoux (top plot) and the Euville (bottom plot) during the core's alteration. Mass dissolution is computed using the X-Ray radiography monitoring and the final core's porosity estimated using the core 3D tomography after alteration.

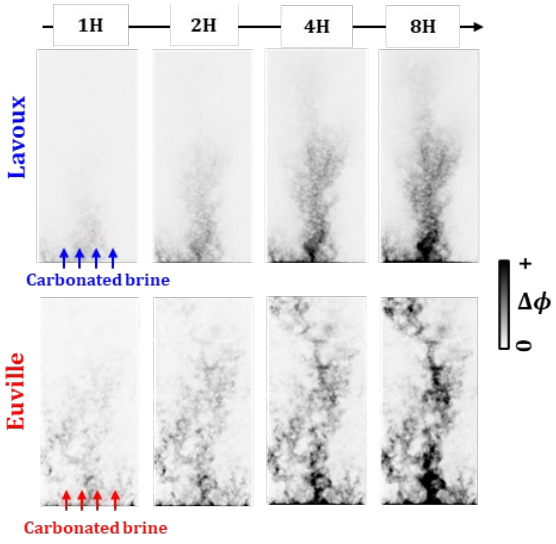

Fig. 11 : Radiography monitoring of the core's alteration during the injection of the carbonated water. Darker shades indicate higher increase of porosity. Injection is performed vertically from bottom to top.

Fig. 12 shows a reconstructed slice of the Lavoux and Euville after alteration (top images) and the subtraction of before and after the alteration to better show the dissolved calcite (bottom images). The dissolution is not radially homogeneous but highly localized in some sections of the slice. This localization seems more important for the Euville, with less but wider paths of dissolution. This pattern favors the transport of the carbonated brine through the core with reduced contact time with the solid matrix. It might explain the earlier breakthrough observed for the Euville. The tracer experiments have demonstrated that the entire core's porous mediums (micro- and macro-systems) was accessible by the fluid, and that it could be invaded within 30 minutes at a comparable flowrate (Fig. 7). The absence of dissolution in some areas of the cores can either be explained by locally lower dissolution rates or because the brine is already equilibrated when flowing through these areas.

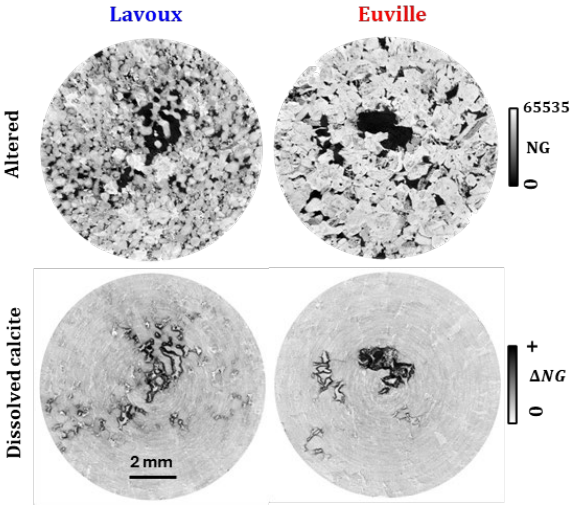

Fig. 12: 3D tomographies (5 µm resolution) of the Lavoux and Euville after alteration (top images). Bottom images show the subtraction of before and after alteration. The reconstructed slices are taken at the same height for the two cores (6 mm from inlet). On the top images, the grey level variations show micro-porosity variations (darker shades show more micro-porous materials). On the bottom images, the grey level variations show the quantity of calcite dissolved (darker shades show more calcite dissolved).

Fig. 13 and Fig. 14 compare the dissolution of porous and less porous materials for the Lavoux and the Euville respectively. Fig. 13 shows a 200 µm ooids (arrow 2) completely dissolved while a calcite crystal next to it (arrow 1) is only dissolved over a thin layer. Comparable observations are made for the Euville, where porous materials at the center of the image (arrow 2) are dissolved while the surrounding material is less dissolved. For these two examples, the porous and less-porous materials are in contact with the same fluid, so the observed differential dissolution cannot be explained by one material being in contact with a less reactive fluid. These observations suggested that the dissolution rate is substantially higher in the micro-porous materials. These observations directly support the controlling role of S_{react} in Eq. 3. This property is difficult to measure locally, but one can easily imagine that micro-porosity generates orders of magnitude more surfaces than the macro-porosity.

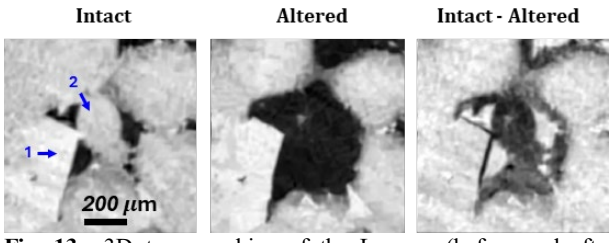

Fig. 13 : 3D tomographies of the Lavoux (before and after alteration, and the subtraction of before and after) comparing the dissolution of micro-porous ooids (arrow 2) and a non-porous calcite crystal (arrow 1). On the left and center images, the grey level variations show micro-porosity variations (darker shades show more micro-porous materials). On the right image, the grey level variations show the quantity of calcite dissolved (darker shades show more calcite dissolved).

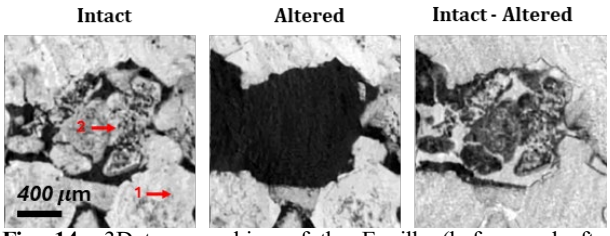

Fig. 14 : 3D tomographies of the Euville (before and after alteration, and the subtraction of before and after) comparing the dissolution of porous materials (arrow 2) surrounded by a less porous grain (arrow 1). On the left and center images, the grey level variations show micro-porosity variations (darker shades show more micro-porous materials). On the right image, the grey level variations show the quantity of calcite dissolved (darker shades show more calcite dissolved).

3.3 Petrophysical characterisation after alteration

The core permeabilities $K_{w,f}$ have been remeasured after the alteration with carbonated water. It is measured to 227 mD for Lavoux and to 3500 mD for Euville. The final total porosity $\phi_{tot,f}$ have also been estimated using the 3D tomographies images. It is computed to 30.1% for Lavoux and 25.8% for Euville. The altered properties ϕ_{totf} and $K_{w,f}$ are summarized in . A different behavior can be observed for the two cores regarding the evolution of the initial permeability. For the Lavoux, the initial permeability has been multiplied by less than 2, while it has been multiplied by more than 100 for the Euville (). In addition, the average dissolution rate was measured higher for the Lavoux, leading to more dissolution and pore space creation.

Table 7: Cores main characteristics after alteration.

Sample	Lavoux	Euville
$K_{w,f}$ **(md)**	226 (K_w*1.7)	3500 (K_w*107)
$\phi_{tot,f}$	30.1% (+5.1%)	25.8% (+5.4%)

Results of the tracer injections performed after alteration are shown in Fig. 15 and Fig. 16. The Lavoux tracer curve shows that it now takes 2h to saturate the core

with the KBr solution, while it took 30 min prior to the alteration. For the Euville the situation is worse as the core saturation with KBr has not been reached after 600 min of injection. The saturation maps shown in Fig. 16 clearly show the preferential invasion of the KBr in the more permeable areas of the core. The dissolution was more localized for the Euville leading to more permeable altered areas, and the micro-porous grains were also initially less permeable for the Euville. This leads to a higher permeability contrast between the altered and non-altered matrix for the Euville than for the Lavoux. These tracer data have not been fitted using the Coats and Smith model as it no longer applies to describe the porous mediums.

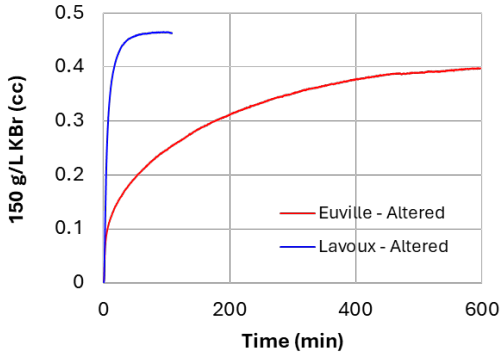

Fig. 15 : Tracer curves of the cores during the miscible displacement of the 150 g/L KBr solution, for the Lavoux (bleu) and Euville (red) samples after alteration.

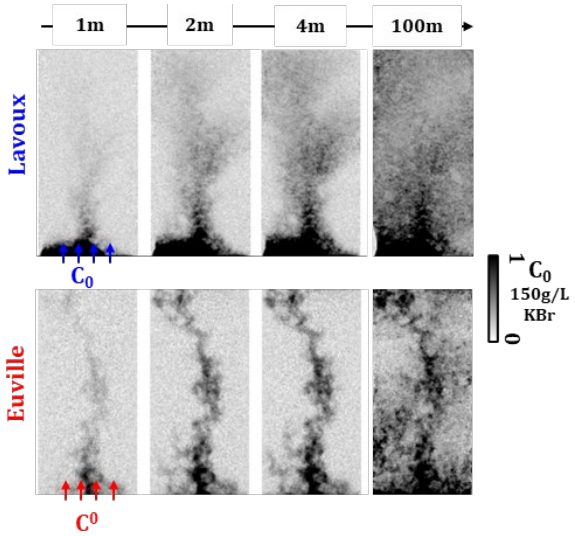

Fig. 16 : 2D saturation maps (radiography monitoring) during the first steps of the tracer injections for the Lavoux (top) and the Euville (bottom) samples after alteration. Injection is performed vertically from bottom to top. Darker shades indicate higher tracer concentrations.

4 Discussion

4.1 Micro-structures

Observations have demonstrated that although the two limestones studied here have a similar chemical composition (almost pure calcite), they have differences in their micro- and macro-porous textures that led to a completely different behavior when in contact with carbonated water. The 3D tomographies have shown that the two samples have a comparable macro-porosity value (between 15% and 16%), but it is organized differently, with less but wider pores for the Euville (Fig. 1). This is the consequence of the larger Euville's crinoids' fragments compared to the Lavoux's ooids. On the other hand, the Lavoux's ooids are three times more micro-porous than the Euville's crinoids' fragments (Fig. 6). The higher permeability measured for the Lavoux despite its thinner macro-pores suggest a major contribution of its micro-porous ooids to the flow. This has been confirmed using the miscible KBr injection and the numerical simulations (Fig. 9). Mass transfer between the micro- and the macro-porosity systems is substantially more effective for the Lavoux than for the Euville (Table 4). Wider and less porous grains are mass transfer limiting, especially when diffusion might be the dominant flow regime to access the micro-porosity. Access for the fluids to the micro-porosity is a key aspect of the reactive transport as it is where most of the reactive surfaces is. In addition to a more connected (or accessible) micro-porous system, Lavoux has twice as much effective surfaces than Euville, and therefore potentially a lot more reactive surface. The more reactive surfaces, the higher the dissolution rate, and the more permeable, the quicker fresh reactive fluid is brought in contact with these surfaces, maintaining the dissolution rate at high levels.

4.2 Core vs local dissolution kinetics

Despite Lavoux potentially higher dissolution kinetics, the core's scale calcite dissolution rate is equivalent for the two cores during the early steps of the displacement (before BT). It was measured to 700 mg/L, or $2.92*10^{-9}$ mol/s when considering the 0.1 cc/min injection flow rate. This value is comparable to the value v_{diss}^{eq}, estimated when considering a transport-limited dissolution rate. Counterintuitively, the core scale dissolution rate is not impacted by the cores' reactive surfaces S_{reac} (before BT): they are not a limiting factor for the dissolution kinetics. Th reason is simple: even if Euville has twice less reactive surfaces than Lavoux, it is here largely enough to equilibrate the reactive fluid during its transport in the core. At the core scale, the dissolution rate is limited by the reactants quantities injected in the cores, which identical for the two cores.

If the core reactive surfaces S_{reac} don't play for the dissolution rate the core scale, it still drives the dissolution rate the local scale, as expressed by Eq. 5. Evidence of local dissolution has shown higher dissolution rates for the micro-porous material for both the Lavoux and the Euville. These micro-porous materials are where most of the reactive surfaces are. In some locations of the cores, ooids or crinoid's crowns have been completely dissolved while adjacent cement have been significantly less dissolved, while in contact with the same fluid and having the same chemical composition (Fig. 13 and Fig. 14).

The dissolution pattern is the physical element here that upscales the local dissolution rate at core scale. As the local dissolution rates are different for Lavoux and Euville, the dissolution patterns grow differently for the cores. For Euville, it moves significantly faster toward the core outlet. This is because the reactive fluid is transported further in the core before being equilibrated, which is the consequence of Euville's lower $S_{sp\alpha}$. Euville's dissolution pattern reached the core outlet after 4h of carbonated water injection, while it hasn't for Lavoux within the 16h of injection. The dissolution BT signs when the dissolution rates are no longer equivalent for the two cores. After BT, the reactive fluid no longer reaches equilibrium before being produced. It causes Euville core scale dissolution rate to decreases after 4h while it stays high for Lavoux.

4.3 Dissolution pattern

In many areas of the cores, even upstream of the dissolution front, most of the micro-porous materials have not been altered at all (Fig. 12). The alteration is highly localized for the two cores, with less but wider paths of dissolution for the Euville. Reactive surfaces is not the only parameter controlling the dissolution pattern. Fluid transport in the macro-porosity system also needs to be understood, as it remains the dominant transport of fresh reactive fluid in the core. It is important to understand that the dissolution pattern advancement is different from the fluid transport. The dissolution pattern only shows where fresh reactive fluids meet calcite. Ahead of the dissolution front, the fluid (flows in the non-altered section of the core.

The dissolution pattern obtained for the Lavoux (Fig. 11) shows some similarities with the first steps of the tracer invasion before alteration (Fig. 8). But such a comparison cannot be made for the Euville: the tracer invasion was homogeneous, yet it leads to a highly localized dissolution pattern. One of the reasons is that the initial rock properties relevant for the reactive transport are changed during the process. Dissolution tends to smooth rugged surfaces, lowering the dissolution rate. It also increases the local permeability, enhancing the initial heterogeneities and modifying the transport of fresh reactive fluids through the core. This last effect is well observed for the Euville using the tracers. Before alteration, the core could be 100% saturated within 30 min while 600 min were not enough after alteration (Fig. 15).

The dissolution pattern observed here using the X-Ray technique is a balance between all these interactions. The Euville and the Lavoux porous medium, despite having some similarities (a dual porosity systems, a connected micro-porosity, identical chemical composition …) don't lead to the same equilibrium. In the Lavoux, most (if not all) of the ooids are highly micro-porous and sufficiently permeable to be accessible to the reactive fluid. In those micro-porous grains, the dissolution rate is orders of magnitude higher than in the macro-pores, enhanced by more reactive surfaces and shorter fluid-to-solid distances. When flowing through the core, the reactive fluid quickly reaches equilibrium upon contact with these ooids. As the channels in the macro-porosity become wider, mass transfer from the macro- to the micro-pores is dampened, allowing the dissolution front to slowly moves forward. The similarity of invasion patterns observed during the tracer injection and the reactive transport for the Lavoux suggests that the dissolution front's progress is partially driven by the initial preferential flow paths.

The situation is different for the Euville as mass transfer from the macro-pores to the micro-pores is limited by the grain's lower connectivity and the wider macro-pores. Consequently, the reactive fluid flows further in the core before being equilibrated with the calcite. Several small wormholes are simultaneously formed, until one of them take over the others, by creating a pathway of least resistance to the flow. As most of the reactive fluid is driven through it, its dominant position is maintained. The crinoids' crowns might contribute to the domination of one wormhole over the others. Observations have shown that this specific type of crinoid' fragments are preferentially dissolved (Fig. 14). This can be explained by their additional intergranular porosity when compared to the more compact crinoid's stalks (Fig. 1). It favors mass transfer between the macro- and the micro-pores, improving the dissolution rate and creating path of higher permeability. It is possible that the spatial distribution of the crinoids' crowns is a key factor for the wormholes progress. The dominant one might be the one that connect most these grains from the core inlet to outlet.

For both the Euville and Lavoux, the contribution of the calcite cement to the reactive transport is ambiguous. It is a non-porous material with no contribution to the flow, therefore leading to locally lower permeabilities. But it also offers less surfaces to the reactive fluids, lowering the local dissolution rate and enabling the reactive fluid to flow further in the core before being equilibrated. Doing so, it also prevents the flow path to get wider by dissolution. The interplay between the cement and the reactive transport could be investigated using numerical simulations and various scenarios of cement spatial distribution.

The previous discussions regarding the calcite dissolution rate and the fluid transport in the porous medium have highlighted the complexity of reactive transport. Results obtained in this study for Lavoux and Euville cores can be interpreted from the perspective of the Péclet and Damköhler classification, without going in details into these two dimensionless numbers construction. Euville core has led to a clear wormhole dissolution pattern, where the transport of the reactive fluid in the micro-porous grains is mass-transport limited. Lavoux's dissolution pattern is a bit more ambiguous, falling between the wormhole type and the compact type. Transport of the reactive fluid is not a limiting factor. In these ooids, the dissolution is driven by the reactive surface, leading to their compact dissolution. But some of them are shielded by calcite cement, dampening the mass transfer to the micro-porosity, and allowing the reactive fluid to be transported along preferential circulation paths. This favors the formation of small wormholes. As for the Euville's crinoid's crowns, the cement spatial distribution in the core is a key aspect of the dissolution control.

4.4 Evolution of the initial rock flow properties

The evolution of the core properties before and after the alteration for the Lavoux and the Euville can be explained with their respective dissolution pattern and a simple assumption of almost null permeability in the core's sections crossed by the wormhole. For the Lavoux, the wormholes have reached half of the core, so the permeability is overall multiplied by 2. For the Euville the wormholes have break through the core, so its resistance to the flow is almost null. The previous statement made here that the alteration behavior is completely different of the two cores might be misleading. If the carbonated water had been injected for 16 additional hours, little changes would have been observed for the Euville as the dissolution rate was already dropping. But the wormholes would have breakthrough for the Lavoux, and its flow properties would have been altered comparably to the Euville ones after 16h of injection. In this study, we have been comparing the alteration after equivalent volumes of carbonated water injected, but not after equivalent advancement of the dissolution progress in the core.

The description made here of Lavoux or Euville dissolution patterns is closely related to the scale of observation. Using the 5 µm pixel resolution tomography data sets (Fig. 12), the two dissolution patterns can be described at the core scale as ramified wormholes, with less branches for the Euville than for the Lavoux. Using the 30 µm radiographies (Fig. 11), the dissolution pattern still appears as localized for the Euville, but it now may be described as diffused for the Lavoux. If a medical CT-scanner had been used with a lower resolution, the distinction between these two patterns might no longer be possible. Inversely, when looking closer at the grain scale, the dissolution is compact whatever the grain type or micro-porosity value.

Conclusions and perspective

Dissolution experiments have been conducted on two limestones (namely a Lavoux and an Euville limestones), that have the same chemical composition (pure calcite) but differ by their porous system architecture. The latter have been characterized through an extensive workflow of experiments, all run using an in-house injection platform (CAL-X™).

Results have shown that:

- The micro-porous architecture plays a key role in determining not only the dissolution rate but also the resulting flow paths, permeability evolution, and dissolution patterns.
- Lavoux limestone, with higher micro-porosity and better-connected grains, showed a more homogeneous and sustained dissolution front, while Euville developed early breakthrough and localized wormholes due to transport-limited conditions in the micro-porous grains.
- The distinction between apparent porosity and effective reactivity underscores the importance of characterizing reactive surface area (S_{reac}) and mass transfer dynamics beyond standard static porosity measurements.
- Our findings challenge the assumption that bulk porosity or initial permeability alone can predict reactive transport outcomes.

Among the future work, we are planning to run Lattice Boltzmann simulations at the core scale. Our code is limited to a monophasic flow simulation in the macro-porosity only. But its comparison with the measured permeability will provide insights to better understand the contribution of the micro-porosity on the total flow. The simulation will also provide the core permeability field. This should contribute to better understand the wormholes formation and propagation in the core. Higher resolution 3D images (0.7 µm pixel resolution) have also been acquired to better describe the micro-porous grains features relevant for the reactive transport. Finally, 3D simulations at Darcy' scale using in-house tools are also planned to fit a geochemical model. This step will require upscaling all properties relevant to the reactive transport at the Darcy' scale. This will be done using the 3D tomography images and results from the Lattice Boltzmann simulations.

References

[1] IPCC, *Global warming of 1.5 C*2018.
[2] P. Kelemen, S. M. Benson, H. Pilorgé, P. Psarras, and J. Wilcox, Front. Clim., 1, (2019).
[3] UNEP, "The emissions gap report 2017: A UN environment synthesis report,"2017.
[4] National Academies Press (US), *Negative emissions technologies and reliable sequestration: A research agenda*. Washington DC: The National Academies Press2019.
[5] H. de Coninck and S. Benson, Annual Review of Environment and Resources, 39, 243, (2014).
[6] M. A. Amooie, M. R. Soltanian, and J. Moortgat, Phys. Rev. E, 98, (2018).
[7] L. N. Plummer, T. M. L. Wigley, and D. L. Parkhurst, American Journal of Science, 278, 179, (1978).
[8] G. Daccord, O. Liétard, and R. Lenormand, Chemical Engineering Science, 48, 179, (1993).
[9] G. Daccord, R. Lenormand, and O. Liétard, Chemical Engineering Science, 48, 169, (1993).
[10] F. Golfier, C. Zarcone, B. Bazin, R. Lenormand, D. Lasseux, and M. Quintard, Journal of Fluid Mechanics, 457, 213, (2002).
[11] H. P. Menke, J. Maes, and S. Geiger, Scientific Reports, 13, (2023).
[12] T. Briolet, E. Bemer, O. Sissmann, and J. Fortin, Geochimica et Cosmochimica Acta, (2025).
[13] M. Mascle *et al.*, Petro S Journ, 66, 26, (2025).
[14] Y. Mäkinen, L. Azzari, and A. Foi, IEEE Transactions on Image Processing, 29, 8339, (2020).
[15] S. Youssef, M. Mascle, and O. Vizika, (2018).

[16] M. Mascle, E. Rosenberg, B. Roboele, E. Kowalewski, and S. Youssef, Oil Gas Sci. Technol. – Rev. IFP Energies nouvelles, 76, (2021).
[17] K. H. Coats and B. D. Smith, Society of Petroleum Engineers Journal, 4, 73, (1964).
[18] S. Brunauer, P. H. Emmett, and E. Teller, Journal of the American Chemical Society, 60, 309, (1938).